Eikonal surface wave tomography of central and eastern China

Pengxiang Zhou, Sébastien Chevrot, Maximilien Lehujeur, Shaohong Xia, Chunquan Yu

Geophysical Journal International

Geophys. J. Int. (2022) **231,** 1865–1879
Advance Access publication 2022 August 6
GJI Seismology

https://doi.org/10.1093/gji/ggac296

Eikonal surface wave tomography of central and eastern China

Pengxiang Zhou [1,2,3], Sébastien Chevrot [3], Maximilien Lehujeur,[3,4] Shaohong Xia [2,5] and Chunquan Yu [1,5]

[1] *Department of Earth and Space Sciences, Southern University of Science and Technology, Shenzhen,* 518000, *China*
[2] *CAS Key Laboratory of Ocean and Marginal Sea Geology, South China Sea Institute of Oceanology, Chinese Academy of Sciences, Guangzhou,* 510000, *China E-mail: shxia@scsio.ac.cn*
[3] *GET, UMR* 5563, *Observatoire Midi Pyrénées, Université Paul Sabatier, CNRS, IRD, CNES, Toulouse,* 31400, *France*
[4] *GERS-GeoEND, Université Gustave Eiffel, Bouguenais,* F-44344, *France*
[5] *Southern Marine Science and Engineering Guangdong Laboratory (Guangzhou), Guangzhou,* 510000, *China*

Accepted 2022 August 2. Received 2022 July 7; in original form 2021 September 3

SUMMARY

Eikonal tomography has become a key approach to image lithospheric structures with surface waves recorded by dense regional arrays. Its main advantage is that phase velocities can be determined directly from phase measurements without resolving a tomographic inverse problem. Here, we apply a new smoothing spline eikonal tomography approach to a selection of 40 large (M_w larger than 6.5) teleseismic events recorded by the permanent seismic stations of the CEArray. We first apply a time–frequency filter to isolate the fundamental mode of Rayleigh waves and cross-correlate the cleaned and isolated surface wave records to measure precise relative traveltimes. The phase measurements are then unwrapped and corrected for cycle skipping. Finally, we derive phase-velocity maps from the gradient of the reconstructed traveltime fields, using the eikonal equation. We obtain finely resolved phase-velocity maps from 25 to 150 s period that are inverted to obtain a 3-D shear wave velocity model which is in good agreement with previous tomographic studies. The lithospheric architecture emerging from the phase-velocity maps and 3-D *S*-wave velocities correlates with surface geology and major tectonic provinces. In particular, the architecture of the narrow rift systems, the South China Craton, and the North China Craton (NCC) are revealed with unprecedented details. The South China Craton is characterized by very high velocities beneath the Sichuan Basin. The NCC shows more complex structures with two high-velocity anomalies beneath the Ordos Basin and the southeastern NCC and low-velocity anomalies beneath the Cenozoic rift systems.

Key words: Image processing; Seismic tomography; Surface waves and free oscillations; Cratons.

Key words:; Eikonal tomography.

1 INTRODUCTION

The present-day tectonic evolution of eastern Asia is driven by the Pacific plate subduction to the east and the India-Asia continental collision to the west. The Mesozoic–Cenozoic destruction of the lithosphere in eastern China (Menzies *et al.* 1993; Griffin *et al.* 1998; Menzies & Xu 1998; Wu *et al.* 2005) and the Cenozoic rise of the Tibetan Plateau (TP, Yin & Harrison 2000; Yin 2006) are the two most significant recent tectonic events. As the major part of eastern Asia, central and eastern China are composed of Precambrian cratonic blocks and large Phanerozoic orogenic belts, such as the North China Craton (NCC) in the north, the South China Craton (SCC) in the south, the Qinling–Dabie orogenic Belt (QD) between the NCC and SCC, and the Tibetan–Himalayan orogenic system in the west. Inside the NCC, two major Archean and Palaeoproterozoic blocks (the WNCC and ENCC) are separated by a Palaeoproterozoic orogen (the Trans North-China Orogen, TNCO), with a transition that is strongly expressed in both topography and gravity (Fig. 1). The amalgamation of the ENCC and WNCC along the SW–NE trending TNCO resulted in the cratonization of the NCC (Zhao *et al.* 2005). The SCC consists of the late Archean to Palaeoproterozoic Yangtze Craton (YZC) to the northwest and the Neoproterozoic Cathyasia

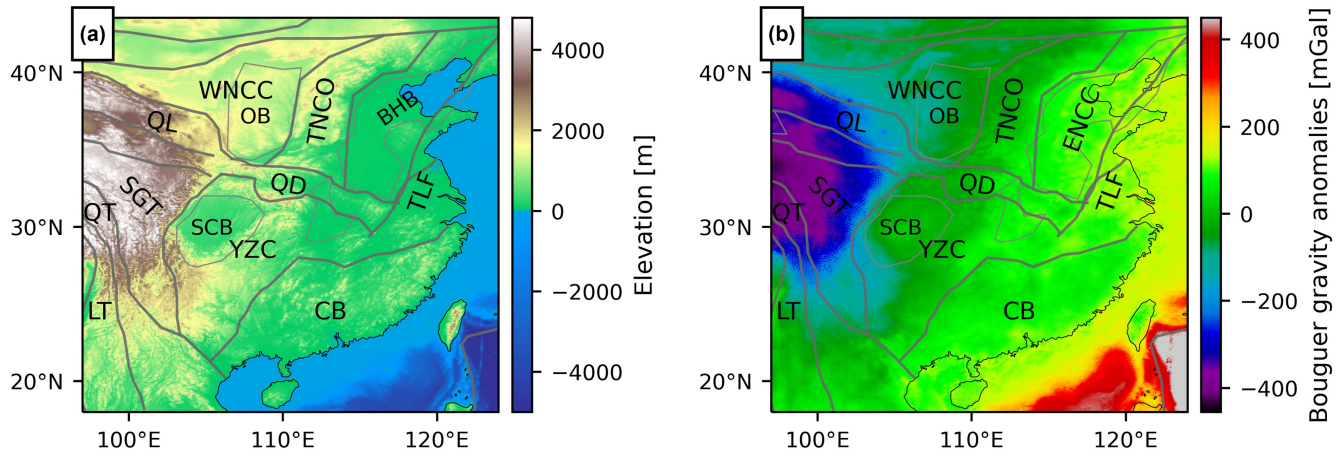

Figure 1. (a) Topographic and (b) gravity maps of continental China with major tectonic boundaries represented by grey lines. The abbreviations design Western North China Craton (WNCC), TNCO, Eastern North China Craton (ENCC), Bohai Basin (BHB), OB, QD, YZC, Cathaysia Block (CB), Qilian Orogenic Belt (QL), Songpan-Ganzi Terrane (SGT), Qiang-tang Terrane (QT), Lhasa Terrane (LT), Sichuan Basin (SCB) and Tanlu Fault (TLF).

Block (CB) to the southeast. The two blocks collided and merged into the SCC during the Neoproterozoic (Zhao & Cawood 1999, 2012; Fig. 1).

By the end of 2007, a new digital seismic monitoring system aggregated the different provincial seismic networks (Zheng *et al.* 2010). Hereafter we will refer to this permanent nationwide array as the CEArray, following Zhou *et al.* (2012). Central and eastern China are the most densely covered regions (Fig. 2). Many tomographic studies have exploited the CEArray records to image crustal and mantle structure with body waves (e.g. Liang *et al.* 2004; Huang & Zhao 2006, and references therein) as well as surface waves (e.g. Feng & An 2010; Li *et al.* 2013b; Xu *et al.* 2013; Pandey *et al.* 2014, and references therein). These studies have greatly improved our understanding of the tectonic history of eastern Asia, but many controversial problems remain open. For example, whereas the SCC and NCC are both Archean cratons, the former is very stable but the latter is characterized by a very active seismicity. Different models have been proposed to explain the evolution and destruction of the NCC (Zhu *et al.* 2012; Sheldrick *et al.* 2020; Xia *et al.* 2020). Discriminating these different models requires tomographic images of lithospheric structures with a finer resolution than currently available.

The main purpose of this study is to obtain finely resolved phase-velocity maps (25–150 s) and 3-D shear wave model of continental China. We use an improved version of eikonal tomography (Chevrot & Lehujeur 2022) that exploits the phase of Rayleigh waves recorded by the CEArray. The method consists in measuring phase velocities from the gradient of the phase surface reconstructed from smoothing spline interpolation of phase measurements at the position of the stations. Because eikonal tomography avoids resolving a tomographic inverse problem, it is thus both simpler to implement and more robust than classical tomographic approaches. In addition, it requires less regularization constraints such as damping and smoothing, which inevitably degrade the spatial resolution of tomographic images. The critical issues become data selection and phase measurement.

The paper is organized as follows. We begin with a brief description of eikonal tomography in Section 2. We then detail our data selection and phase measurement procedures in Section 3, as well as our method to unwrap these phase measurements and reconstruct Rayleigh wave fronts across China. In Section 4, we describe our smoothing spline interpolation scheme performed in spherical coordinates. Using the eikonal equation, the reconstructed phase fields are exploited to obtain phase-velocity maps for periods between 25 and 150 s. In Sections 5 and 6, we invert the phase-velocity maps into a 3-D *S*-wave model. In Sections 7 and 8, we present interpretations of the newly resolved model, and discuss several implications of our results.

2 EIKONAL TOMOGRAPHY: METHODOLOGY

This section summarizes the relevant aspects of eikonal tomography. For further details, we refer the reader to Lehujeur & Chevrot (2020a,b). In a smoothly varying Earth model, the displacement of a single surface wave mode at a single frequency satisfies the Helmholtz equation (e.g. Tromp & Dahlen 1992; Wielandt 1993):

$$\frac{1}{c^2} = \nabla T^2 + \frac{\Delta A}{\omega^2 A}, \tag{1}$$

where c is the local Love or Rayleigh wave phase velocity, T and A are respectively the phase and amplitude, ω the angular frequency and Δ the Laplacian operator. Therefore, if the phase and amplitude fields of surface waves are known, the phase velocity can be directly derived from the Helmholtz equation. The amplitude correction term involves the Laplacian of the amplitude, which is challenging to compute. However, Lehujeur & Chevrot (2020a,b) have demonstrated that phase velocities can be derived from the eikonal equation (Lin *et al.* 2009)

$$\frac{1}{c^2} = \nabla T^2 \tag{2}$$

by averaging the results obtained with different wave fronts arriving from different backazimuths. Eikonal tomography is thus simpler to implement because it does not require the amplitude correction term and because it does not involve resolving a tomographic inverse problem. In addition, it also avoids imposing regularization constraints on the model, which can potentially degrade the spatial resolution. The critical steps become the data selection and the reconstruction of the traveltime surfaces from a discrete number of phase measurements performed at the station positions.

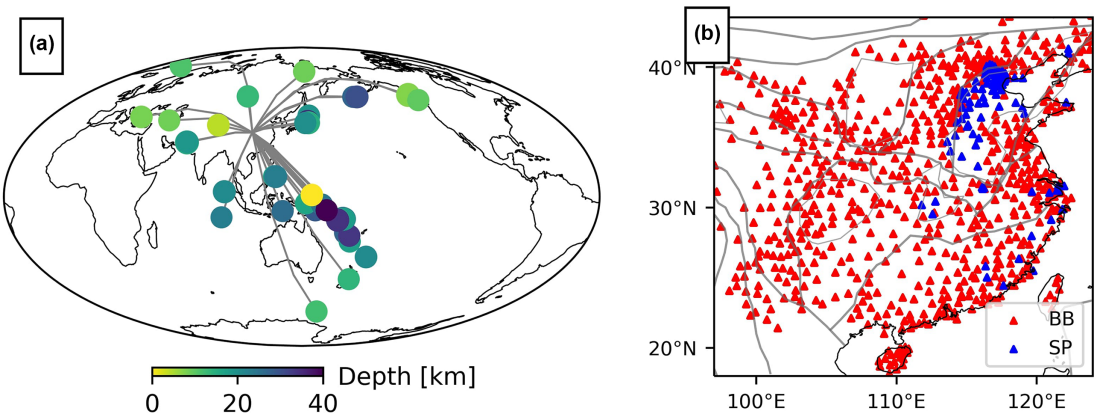

Figure 2. (a) Teleseismic events used in this study. Focal depths are represented by coloured circles and great-circle ray paths to the array centre by grey lines. (b) Broad band (red triangles) and SP (blue triangles) station distribution.

Recent applications of eikonal tomography relied on splines in tension to reconstruct traveltime surfaces by spatial interpolation (e.g. Lin *et al.* 2009; Lin & Ritzwoller 2011; Feng & Ritzwoller 2019). However, splines in tension impose that phase measurements are matched exactly at the station positions. This can produce spurious oscillations in the interpolated traveltime surfaces, especially if the station distribution is uneven with large variations of interstation distances. In addition, the zero-curvature phase boundary condition may not necessarily be consistent with the wave equation. For these reasons, Chevrot & Lehujeur (2022) proposed to use smoothing splines to reconstruct the traveltime surfaces. Smoothing splines search for the best compromise between fitting the observed phase and the wave equation. With this approach, robust and stable phase-velocity maps are obtained after ∼20 wave fronts arriving from different azimuths. Adding more events did not significantly change the final average phase-velocity maps.

In this study, we apply the smoothing spline interpolation method of Chevrot & Lehujeur (2022) to the Rayleigh waves generated by 40 large teleseismic events recorded by the dense CEArray. Because the region considered in this study, continental China, is quite large, we used the modified version of their algorithm expressed in spherical coordinates. The different steps involved in our implementation of eikonal tomography are described in the next section.

3 DATA PROCESSING AND PHASE MEASUREMENT

Seismic data used in this study come from the CEArray, which comprises medium-band (cut-off period of 20, 40 and 60 s), broad-band (cut-off period of 120 s) and ultra broad-band stations (cut-off period of 360 s, collectively referred to as BB), as well as a small number of short-period stations (cut-off period of 1–2 s, SP), for a total of nearly 900 stations (Fig. 2b). We kept the broad-band records of 40 shallow (depth $<$ 40 km) teleseismic events in the period 2008–2014 with magnitude (M_w) greater than 6.5. The epicentral distances from the centre of the array range from 20° to 100° to avoid near-source effects and interference from higher modes of Rayleigh waves (Hariharan *et al.* 2020, 2022). Most events are located in the Pacific (Fig. 2a). The information on the earthquake origin time, location and magnitude, were extracted from the ISC catalogue (Fig. 2).

3.1 Data selection and preparation

The vertical component records are first deconvolved from the instrumental response to correct for variations of phase and amplitude caused by the different types of sensors, and then detrended and resampled at 1 Hz.

For each earthquake, we calculate correlation coefficients between all station pairs, including autocorrelation, and wrote these coefficients into a 2-D $N\times N$ correlation matrix, with N the number of stations that have recorded the earthquake. We then compute column averages to obtain a vector containing N average correlation coefficients.

Our first selection criterion is to reject a record if

$$abs\,(c\,[i] - c.\text{median}) > \text{threshold} * c.std,$$

where *c[i]* designs the average correlation coefficient for station *i*, *abs* the absolute value and *std* denotes the standard deviation.

We then considered the energy and dominant frequency of all traces and used the same criterion for the identification of outliers. The thresholds for the three criteria (correlation coefficient, energy and dominant frequency) are set to 3, 3 and 5, respectively. Broad-band and SP seismograms are screened separately according to these three criteria. After quality control, 33 753 traces were preserved from an original data set of 41 145 traces.

3.2 Fundamental mode extraction

We isolate the fundamental mode of Rayleigh waves (R0) by the frequency–time analysis (FTAN) described in Bensen *et al.* (2007). We first extract dispersion curves of group velocity on each record by picking the local maximum amplitudes on dispersion spectrograms. A time–frequency phase-matched filter based on the dispersion curve is then applied to the raw waveforms to extract the fundamental mode and remove multipathing effects. Fig. 3 shows an example of a Rayleigh wave recorded by station GGS before (black line) and after (red line) phase-matched filtering. The filter was built from the dispersion curve picked on the dispersion diagram shown in Fig. 3(b).

It is often difficult to pick dispersion curves from dispersion diagrams. In addition, because our data set is large, with more than 30 000 waveforms recorded by nearly 900 stations, picking the dispersion curves cannot be done manually. To improve the signal-to-noise ratio and automatize the dispersion measurements, we compute local averages of dispersion diagrams, considering the up to

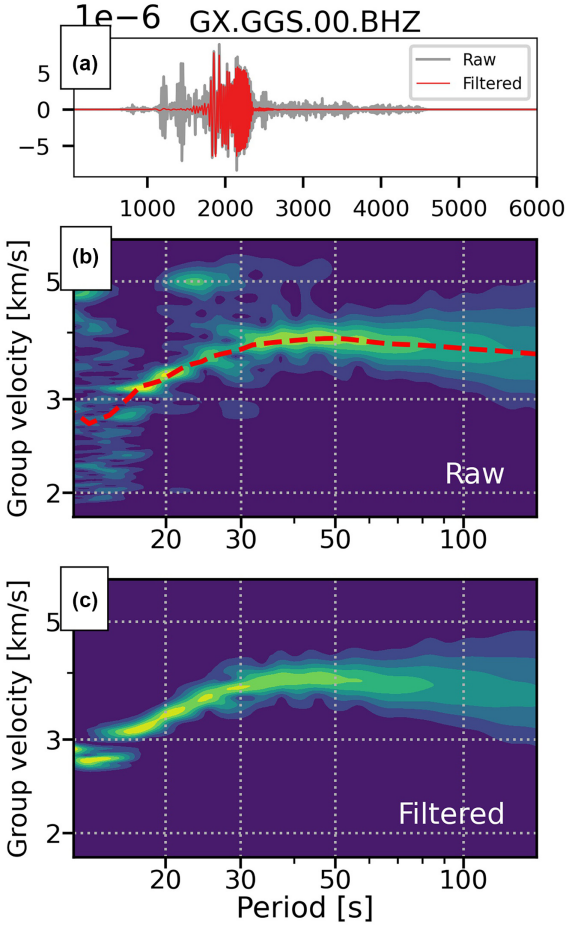

Figure 3. Time–frequency filtering for the isolation of the fundamental mode. The 2013 February 07 M_w 6.7 Solomon event was recorded by station GGS. (a) Vertical component seismograms before (black) and after (red) applying the isolation filter. (b) Spectrogram of the raw waveform. Dashed red line indicates the picked group velocity dispersion curve. (c) Dispersion diagram after filtering.

20 closest stations within 200 km from each station (Figs 4a and b). The dispersion diagram is much cleaner after stacking spectrograms from nearby stations. The automatic extraction of dispersion curves is thus greatly simplified and much more robust. Note that at this point the dispersion curves do not need to be very precise because they are only used for extracting the fundamental mode and cleaning the waveforms.

We then decompose the signal in the Fourier domain in order to obtain a collection of sinusoidal time functions for each frequency. Each sinusoid is tapered with a Gaussian function centred on the picked arrival time of the surface wave at each frequency. The width of the filter is given by a fixed multiple of periods (5 here), so that the taper is broader for lower frequencies. We then reconstruct the filtered signal by simply summing the filtered sinusoids. After filtering, both body and coda waves have been suppressed (Figs 4c and d).

3.3 Traveltime measurements

We measure inter-station phase delays by cross-correlating the filtered waveforms (Fig. 5a). The cross-correlation functions (CCFs) are then tapered with a narrow Gaussian function and the relative traveltimes are read from the maxima of the CCFs at each period. Even with carefully selected data, traveltime differences measured by cross-correlation can be biased by cycle skipping. This problem is particularly serious at high frequency or for stations that are far apart, as in this study. To resolve cycle ambiguities, we use an approach that exploits additional information coming from the other stations in the array and from the lower frequencies, which are less severely affected by this problem.

We first process the CCFs starting from the lowest frequency and progressively considering higher and higher frequencies. We start our analysis at 150 s period. At such a long period, any cycle skip is easily detected and corrected for. Moving to 130 s, the next shorter period considered, we compare the delays measured at this period to those measured at 150 s and correct them by the adequate number of cycle skips so that they fall within one period from the ones measured at 150 s (Fig. 5b). The same procedure is repeated successively for periods 110, 90, 70, 50, 40, 30 and 25 s, and for each pair of stations. Note that SP stations (cut-off period of 1–2 s) were only used for periods below 50 s. The traveltime delays are then stored in a 2-D $N \times N$ matrix (Fig. 5c). At this step, some cycle skipping may still be present, as can be seen in Fig. 5(c) (vertical and horizontal stripes).

In a second step, we determine by linear regression the average traveltime versus distance curve (t–d curve, distance with respect to earthquake sources) for each frequency using all the stations that recorded the particular event considered (Figs 5d and e):

$$t - t' = s*\left(d - d'\right) + n*T + o, \tag{3}$$

where t and d represent time and distance at sampling points, t' and d' the reference point, s the slope, n the number of cycle skips, T the period and o the possible error of the reference point. Multiplying by $\omega = 2\pi/T$ and taking the cosine of the resulting expression leads to

$$\cos\left(\omega*\left(t - t'\right)\right) = \cos\left(\omega*\left(s*\left(d - d'\right) + o\right)\right). \tag{4}$$

We use a grid search to find the optimal combination of s and o that minimizes the observed and predicted t–d curves. This grid search is performed twice, covering s in the range 2–5 km s^{-1} and o within a half-period during the first grid exploration. In the second grid search, the ranges for s and o are respectively reduced to 5 per cent and 10 per cent of their first searched values. Traveltimes are then corrected by an integer number of cycle skips $n = (t^{\text{obs}}\text{-}t^{\text{fit}})/T$, where t^{fit} is the time obtained after the two grid searches. We can see from Figs 5(c) and (f) that the T matrix becomes much smoother after spatial correction, which testifies the quality of our traveltime field estimations (Fig. 5).

An example of traveltime measurement at 50 s period is shown in Fig. 6. The cross-correlation coefficient matrix (Fig. 6e), obtained by correlating each pair of traces, is indeed a very good quality indicator. Most stations show large average correlation coefficients (> 0.9), whereas some stations are clearly less correlated with the other stations. These stations are easily identified by the vertical and horizontal green stripes in Fig. 6(e) or in the map showing station correlation coefficients (Fig. 6f). We use the coefficient matrix as a proxy for measurement quality and eliminate stations that have an average correlation coefficient smaller than 0.5. The remaining measurements are then used to reconstruct the traveltime surfaces of the wave fronts (Fig. 6).

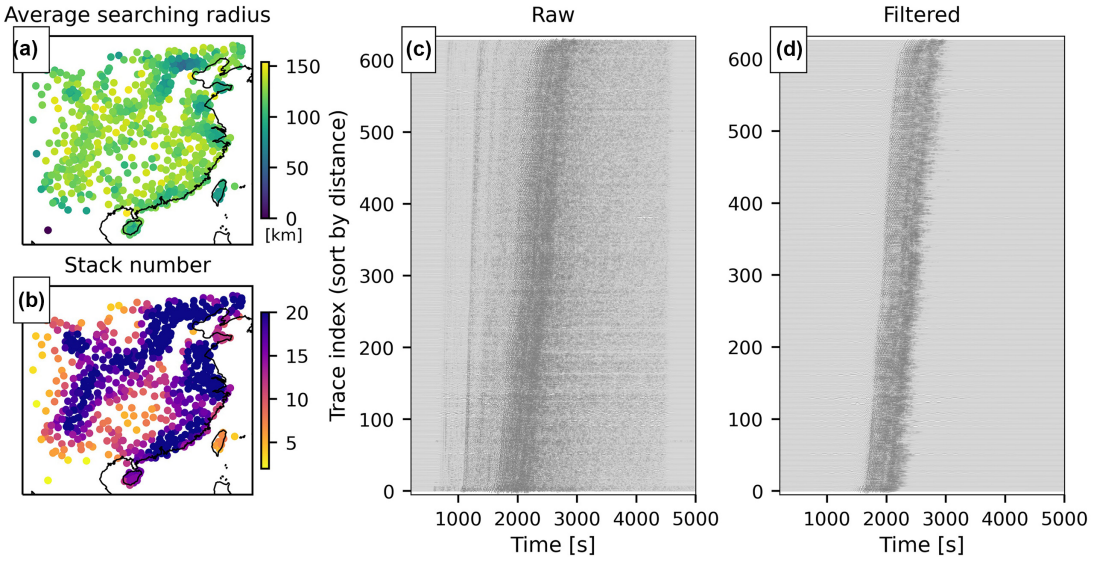

Figure 4. Filtering of Rayleigh waves on the 2013 February 07 M_w 6.7 Solomon event. (a) Average radius for spectrogram averaging at each station. (b) Number of spectrograms averaged at each station. (c) Raw vertical component seismic records, low-pass filtered at 10 s. (d) Fundamental mode of Rayleigh waves after time–frequency filtering.

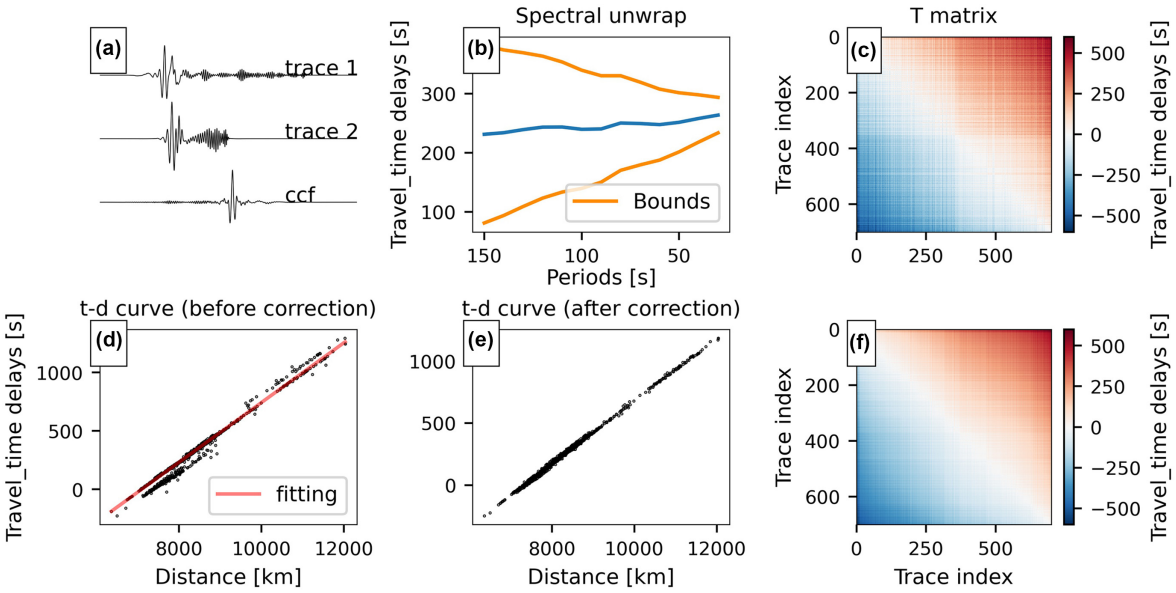

Figure 5. Illustration of the cycle skipping corrections on the 2013 February 07 M_w 6.7 Solomon event. (a) Cross-correlation of two random cleaned traces. (b) Phase unwrapping in the spectral domain. Blue line represents the estimated phase delays from low to high frequency. Orange line indicates the upper and lower boundaries to constrain the estimation. (c) Traveltimes of all traces with all traces (T matrix) at period 50 s. (d) Traveltime delays versus distance distribution before spatial unwrap. Red line indicates the fitting line. (e) Traveltime delays versus distance distribution after spatial unwrap. (f) T matrix after spatial unwrap.

4 INTERPOLATION OF TRAVELTIMES MEASUREMENTS WITH SMOOTHING SPLINES TO RECONSTRUCT TRAVELTIME SURFACES

Before computing the spatial gradient of traveltime fields, we first need to reconstruct traveltime surfaces by interpolating the traveltime measurements onto a regular grid (Figs 7b and c). Interpolation with splines in tension (Smith & Wessel 1990), imposing minimum curvature constraints, has often been used to address this problem (e.g. Lin *et al.* 2009; Lin & Ritzwoller 2011). Here we follow the approach described in Chevrot & Lehujeur (2022), which relies on smoothing splines. The main advantage of smoothing splines is that they offer an optimal compromise between fitting the data and smoothness of the reconstructed traveltime surface. The traveltime surface is obtained by searching for the minimum of the cost function:

$$Q = \frac{1}{N}\left(P \cdot T - T^{\text{obs}}\right)^2 + \frac{\mu}{M}\Delta T^2, \tag{5}$$

where T is the estimated regular traveltimes and T^{obs} is the traveltime field observed at each station, P the sampler to pick the value of T at station locations, μ the regularization parameter, and N and M the number of stations and the number of gridpoints, respectively.

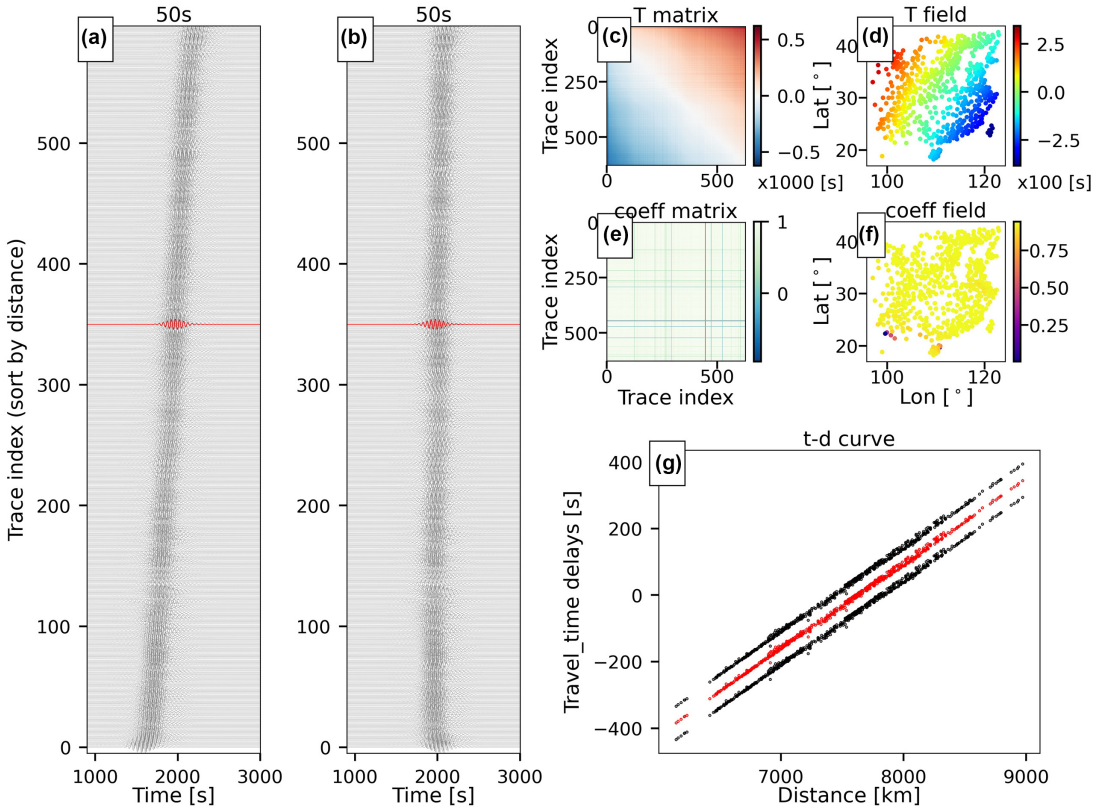

Figure 6. Traveltime measurements for the 2013 February 07 M_w 6.7 Solomon event at 50 s period. Gaussian tapered waveforms (a) before and (b) after phase delay correction. Red traces represent the reference waveform. (c) Traveltime matrix (T matrix) for all pairs of traces cross-correlations. (d) Traveltime (T field) with respect to the reference red traces in (a) and (b). (e) Correlation coefficient matrix (coeff matrix). (f) Correlation coefficient field (coeff field). (g) Traveltime delay versus epicentral distance curve. Red dots represent the estimated values and black dots indicate one period shift of the estimation.

We then search for the traveltime field that minimize Q, for which

$$\nabla Q = 0, \tag{6}$$

under the boundary condition

$$\frac{\nabla T}{\nabla n} = 0, \tag{7}$$

where n denotes the direction orthogonal to the grid boundary.

Choosing the value of the smoothing parameter is still an active topic of research. Whereas Chevrot & Lehujeur (2022) advocate the generalized cross-validation method, here we use a simpler approach which consists in finding the traveltime surface corresponding to a fixed *a priori* value of the norm of the Laplacian (Fig. 7a), whose value has been chosen by trial and error. We thus make the implicit assumption that all surface wave fronts have the same smoothness. The Laplacian is adjusted to balance the fit of traveltime data and the final phase-velocity maps. After performing a first interpolation, we remove stations where the traveltime residual is larger than 1 s (Fig. 7d) and perform a new interpolation, using the same smoothness constraints as in the first interpolation (Fig. 7a).

Fig. 8 shows the residual root-mean-square (RMS) traveltime misfit and the regularization parameter as a function of the average cross-correlation coefficients as defined in Section 3.3 for all events at 50 s period. Fig. 8 also shows that waveform quality does not depend on the magnitude or on the epicentral distance of the event, even though closer events provide records with larger signal-to-noise ratio, and thus are more likely to pass all our quality checks.

5 Phase-velocity maps from 25 to 150 s

After interpolation, from the gradient of the phase traveltime surface in spherical coordinates we can derive the local phase speed as a function of the direction of propagation of the wave (Figs 7f and g). Hence, there is no need to perform a tomographic inversion. For each period, we visually check the quality of phase-velocity maps obtained from the different wave fronts and remove the ones that show patterns with anomalously strong fluctuations. We perform a bootstrap analysis on the final data sets using 10 000 random realizations to derive the final average phase-velocity maps for each period. Errors resulting from neglecting the amplitude correction terms are averaged out by this azimuthal average (Lehujeur & Chevrot 2020b). We finally obtain phase-velocity maps for periods ranging from 25 to 150 s (Fig. 9). At shorter periods, our method fails to provide robust and stable phase measurements, owing to a stronger noise level and greater apparent complexities of seismic waveforms resulting from multipathing. The number of earthquakes kept for each period is shown in Fig. 10.

5.1 Comparison with previous studies

Many surface wave studies have produced dispersion maps or 3-D models in various regions across China. Traditional surface wave tomography using ambient noise or earthquake data has been used to determine crustal- and upper-mantle structures beneath the NCC (Huang *et al.* 2009; Zheng *et al.* 2011; Bao *et al.*

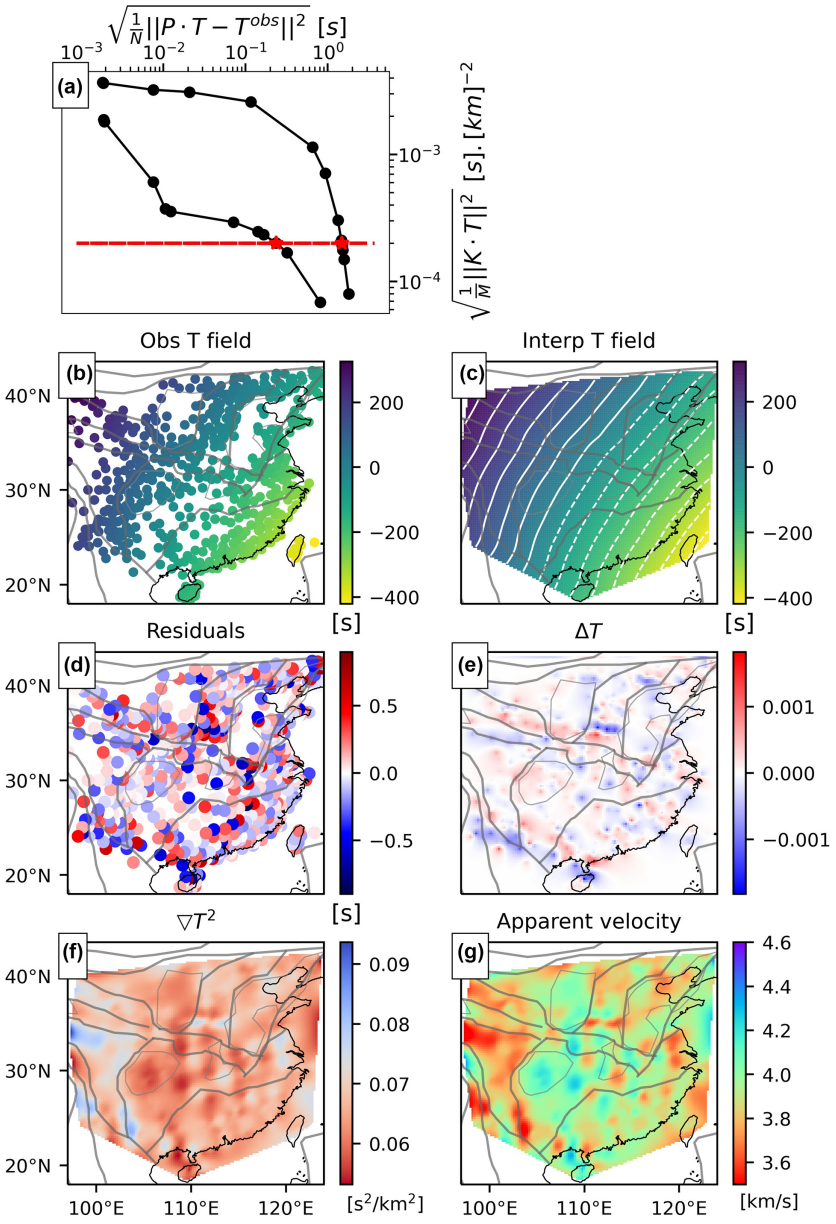

Figure 7. Eikonal tomography procedure for the 2013 February 07 M_w 6.7 Solomon event at 50 s period. (a) Cost balance between the residual and Laplacian term. Dashed red line marks the fixed Lalacian value. (b) Observed traveltime field. (c) Interpolated traveltime field. (d) Residuals between the detrended observed and interpolated traveltime field. (e) Laplacian of the interpolated traveltime field. (f) Gradient of the interpolated traveltime field. (g) Phase-velocity (or apparent velocity) map.

2013), the SCC (Shan *et al.* 2017; Guo *et al.* 2018) and local areas focusing on particular tectonic provinces, such as rift systems (Jiang *et al.* 2013; Ai *et al.* 2019a, 2019b; Cai *et al.* 2021), suture zones and orogens (Zhang *et al.* 2020). Few studies covered the whole continental China (Li *et al.* 2013b; Bao *et al.* 2015; Shen *et al.* 2016). Eikonal/Helmholtz tomography was applied in separate regions of the SCC and NCC (Zhou *et al.* 2012; Hao *et al.* 2021).

We compare in more detail our phase-velocity maps with the classical surface wave tomography of Bao *et al.* (2015), obtained from a much larger data set (more than 700 000 dispersion curves and an even denser network that includes several regional temporary deployments). The comparison with their phase-velocity maps at 25, 50 and 70 s is shown in Fig. 11. To first order, the two models are in remarkable agreement. For instance, the high-velocity anomalies (HVAs) beneath the Ordos and Sichuan basins, which can be related to the cratonic keels of the NCC and YZC, and the low-velocity anomaly (LVA) beneath Tibet, which can be related to the thickened crust, have almost identical geometries in both models. However, small-scale differences can be observed, for example, beneath the CB and Tibet at 70 s. The amplitude of velocity anomalies is smaller in Tibet and YZC in our 25 and 50 s phase-velocity maps. In addition, the small-scale structural details in our maps, for example beneath the NCC, are in remarkable agreement with surface geology, which strongly suggests that they are robust and well resolved.

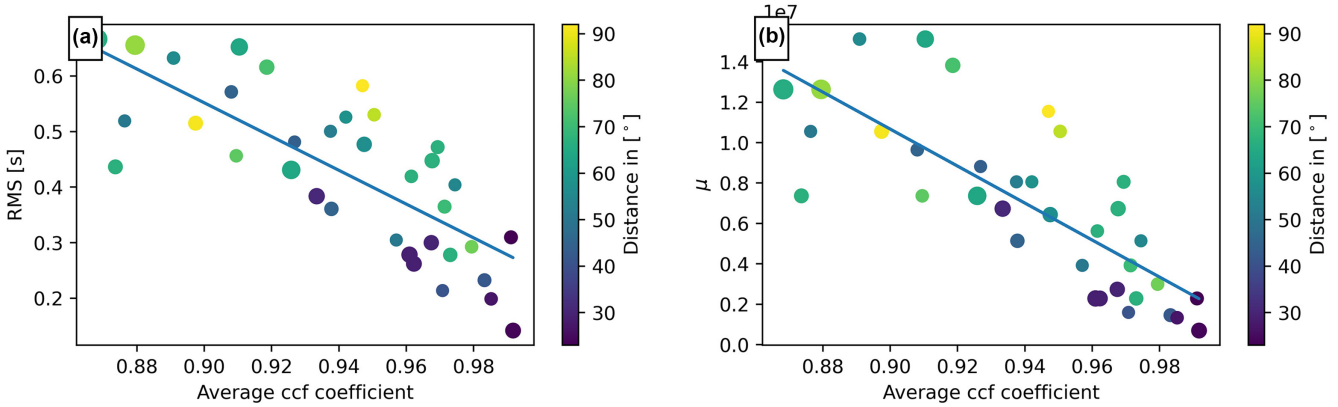

Figure 8. Relationship between waveform quality and interpolation parameters. Solid circles represent earthquakes. (a) Relationship between the average correlation coefficient and the RMS of residuals. Epicentral distance to the array centre is coloured and labelled on the right-hand side of the diagrams. Diameters of circles are proportional to earthquake magnitude. (b) Relationship between the average correlation coefficient and regularization parameter (μ).

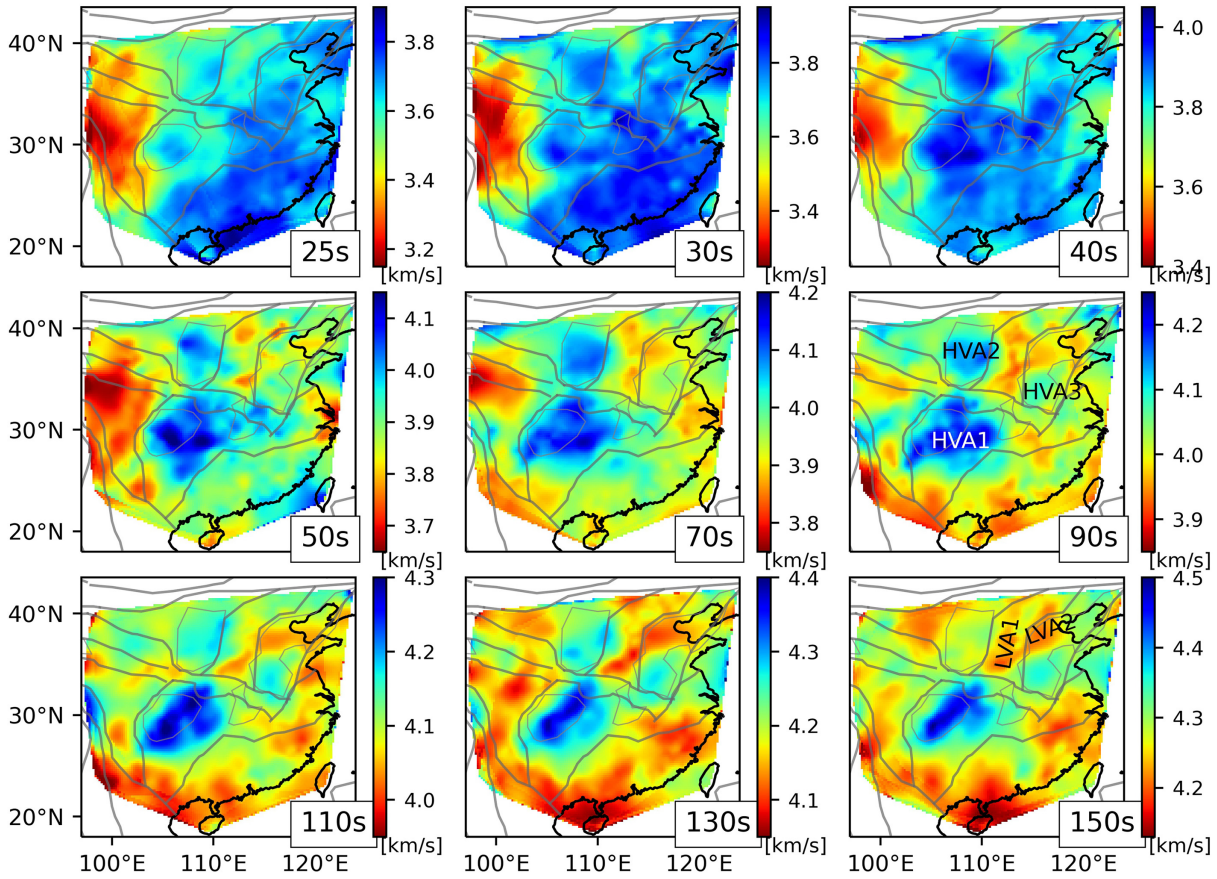

Figure 9. Phase-velocity maps for periods from 25 to 150 s. Major tectonic boundaries and basins are represented with grey lines. HVA: high-velocity anomaly and LVA: low-velocity anomaly.

5.2 The cratonic blocks: North China and South China Cratons

The boundary between high and neutral velocities at 25 s (Fig. 9) correlates with the topography and gravity gradients (Fig. 1). The velocity contrast between Tibet and the western YZC from 25 to 50 s is also consistent with the main tectonic divides. A salient feature in the phase-velocity maps shown in Fig. 9 are the rift systems in the TNCO (the Shanxi rift) and northern ENCC (the Bohai rift). Both have a strong signature at all periods. These LVAs have been imaged in many previous tomographic studies and may reflect ongoing mantle upwelling (Jiang *et al.* 2013; Bao *et al.* 2015; Ai *et al.* 2019a, b). The shapes of these two LVAs closely follow the geometry of the Cenozoic rift systems and distribution of volcanism (e.g. Xu *et al.* 2014), although we observe a clear offset between the southern part of the Shanxi rift and the LVA anomaly in the 50 and 70 s phase-velocity maps, which has been documented in several previous studies (e.g. Jiang *et al.* 2013; Cai *et al.* 2021). We refer to the two LVAs as LVA1 and LVA2 for the former and latter ones

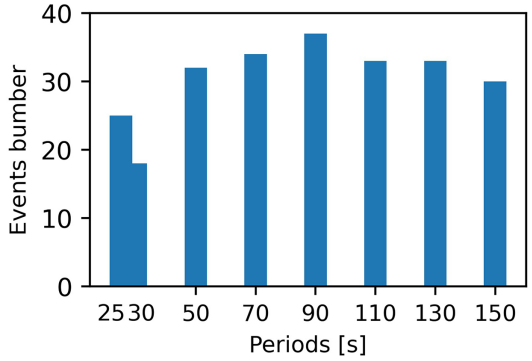

Figure 10. Number of wave fronts used at each period.

based on geological divides, though these two LVAs are spatially connected in our phase-velocity maps (Fig. 9).

Our phase-velocity maps at 50–150 s period reveal the details of the deep architecture of the NCC and the SCC. The most predominant feature in the phase-velocity maps at periods 110, 130 and 150 s is the very deep root (HVA1) beneath the YZC (Fig. 9). Such deep fast velocity roots are not observed in the other parts of the SCC (the eastern YZC, southern YZC and the CB). Another less predominant high velocity anomaly (HVA2) is observed beneath the Ordos basin (OB) in the NCC. This anomaly is less pronounced at long periods, which suggests a different nature of the lithosphere compared to YZC. Another high velocity anomaly (HVA3), located in the southern ENCC, is observed at all periods. Its magnitude at long period (from 110 to 150 s) is comparable to HVA2 underneath the OB. Overall, the deep architecture of the NCC seems rather heterogeneous and shattered compared to the more homogeneous nature of the SCC.

6 SHEAR WAVE VELOCITY INVERSION

To build a 3-D shear wave velocity model, we invert the fundamental Rayleigh wave dispersion curves extracted from each pixel of the phase-velocity maps using a Bayesian framework (Lehujeur *et al.* 2018). We estimate the posterior probability density distribution of the model space with a Metropolis algorithm (e.g. Mosegaard & Tarantola 1995) that combines prior probability density functions (PDF) of the model and data spaces (Tarantola 2005). The quality of a depth model can be written as

$$\mathrm{llk}\,(m) = \log\rho_M\,(m) + \log\rho_D\,(g\,(m))\,,$$

where llk is the logarithm of the likelihood, m is an array of parameters corresponding to a depth model, ρ_M is the prior PDF of the model space, ρ_D is the PDF of the data space and g is the theory function used to compute dispersion curves. Taking the logarithm of the likelihood increases the stability of the Metropolis algorithm. The prior PDF of the model space (ρ_M) is uniform for each parameter of the model (Table 1). The prior constraints on *Vs*, *Vp*/*Vs* and density in each layer are adjusted after the ak135 continental model (Kennett *et al.* 1995; Montagner & Kennett 1996). The prior PDF of the data space (ρ_D) is defined using lognormal probability laws for each point in the dispersion curve, and we assume that the phase-velocity measurements are independent, that is, we use a diagonal data covariance matrix (Tarantola 2005).

To constrain the crustal component, we add phase-velocity measurements for periods between 10 and 22 s taken from Bao *et al.* (2015). For each location, we invert the observed dispersion curves with 12 independent Markov chains running in parallel. The moves between subsequent models explored by the random walk process are governed by a Gaussian proposal PDF, whose covariance matrix is taken as diagonal. The diagonal terms are adjusted during the inversion to stabilize the acceptance ratio of the chains to approximately 25 per cent. We use Herrman's 'Computer Programs in Seismology' suite of code (Herrmann 2013) for the forward computation of the dispersion curves. Each chain runs until 1000 models have been kept. In the end, we select the 1000 best models found by the 12 chains. The median of these 1000 best models is retained as the solution to the inversion (Fig. 12). We then combine the 1-D shear wave velocity models obtained inside each pixel to form a 3-D model (Figs 13–15).

7 RESULTS

Two examples of the posterior probability density distribution for the *S*-wave velocity structure obtained by inverting regional average phase velocities are plotted in Fig 12. The ak135 model (Kennett *et al.* 1995) is also shown for comparison (purple line). In the lower crust of the OB, the regional average model is lower than ak135. In the uppermost mantle, the inversion requires a velocity increase at depth from ∼60 to 150 km. From 150 to 250 km, the regional average *S*-wave velocity is similar to the ak135 model.

Fig 13 plots a series of horizontal slices of the model at different depths. The shallow crustal structure (10 km), related to surface geology, is characterized by the LVAs associated with sedimentary basins, including the Bohai Basin and SCB. High velocities are observed in the orogens, such as the TNCO and QD. Around Moho depth level (30 km), high velocities are observed in the eastern part of the topographic and gravity gradients, and TP shows low velocities. At upper-mantle depths, two HVAs are imaged beneath the OB and inner YZC. Low velocities are observed in the broad region of TNCO, ENCC, eastern and southern YZC and the entire CB. From 170 to 200 km depth, relatively high velocities can be seen in the southern part of the ENCC and the eastern part of the TLF.

Eight cross-sections along latitude and longitude with their corresponding profiles shown in Fig 13 are plotted in Figs 14 and 15. Profile AA′ cuts across the TP and the NCC. High velocities in the uppermost mantle occupy the western part of the TNCO, while the eastern part shows LVAs. Intermediate velocities are observed at around 130 km depth beneath the OB. Section BB′ crosses the TP and the southern NCC. The low velocities below the eastern edge of the TNCO and TLF extend to 200 km depth. Strong LVAs can be seen beneath the eastern YZC. Profile CC′ goes through the TP and YZC. Strong HVAs lie beneath the western YZC. In the middle part, relatively high velocities overlay low velocities. The easternmost part of the YZC show an LVA. Low velocities underneath intermediate velocities can be observed across the profile DD′, which spans the TP, southern YZC and CB. Fig 15 displays sections along latitude. Same patterns can be observed, such as strong high velocities under the YZC and OB in profile FF′, low velocities below the southern TNCO in profile GG′ and Bohai basin in profile HH′.

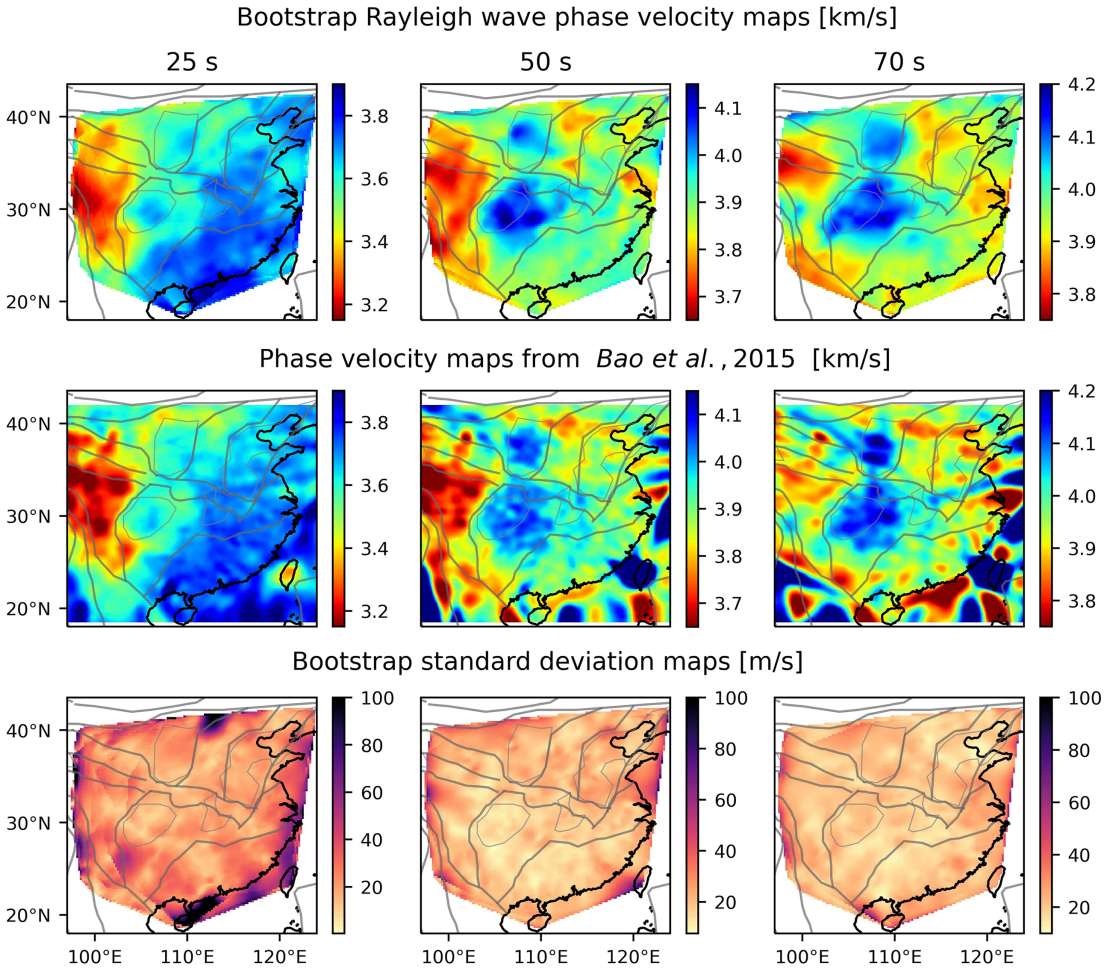

Figure 11. Phase-velocity maps for period 25, 50 and 70 s. The first row is from this study and the second row is derived from Bao *et al.* (2015). The third row shows maps of standard deviation quantified by bootstrap analysis.

Table 1 Prior boundaries of uniform probability distribution for each parameter of the depth model

Layer number	Depth range (km)	*Vs* range (km s^{-1})	*Vp*/*Vs*	Density range (g cm^{-3})
1	0–10	1.50–2.50	2	2.3–2.6
2	5–35	2.86–4.06	1.676	2.6
3	15–85	3.25–4.45	1.688	2.92
4	57.5–97.5	3.88–5.00	1.688	3.6
5	90–140	3.89–5.09	1.79	3.5
6	130–190	3.90–5.10	1.8	3.4
7	180–240	3.91–5.11	1.82	3.35
8	230–300	3.96–5.16	1.838	3.34
Half-pace	300-	4.05–5.25	1.842	3.39

8 DISCUSSION

8.1 Phase-velocity maps derived from eikonal tomography

The phase-velocity maps obtained with our new implementation of eikonal tomography are characterized by fine spatial resolution and lower contamination by artefacts. Long wavelength characteristics are in good agreement with that using more conventional surface wave approaches (Feng & An 2010; Li *et al.* 2013b; Pandey *et al.* 2014; Bao *et al.* 2015). The key aspect of eikonal tomography is to be able to measure traveltimes very accurately. In this study, this is achieved by exploiting the information redundancy offered by the whole seismic array, instead of analysing each record separately. The seismic array is first exploited to build the time–frequency filter to filter the fundamental mode of Rayleigh waves. This filter also removes the effects of scattering, multipathing and interferences with other seismic phases in the seismograms. The cross-correlation matrix also allows us to detect and discard the bad traces. The whole array is used to correct for cycle skipping errors in relative traveltime measurements, a problem that can often occur on data filtered in a narrow frequency band. Finally, the phase-velocity maps

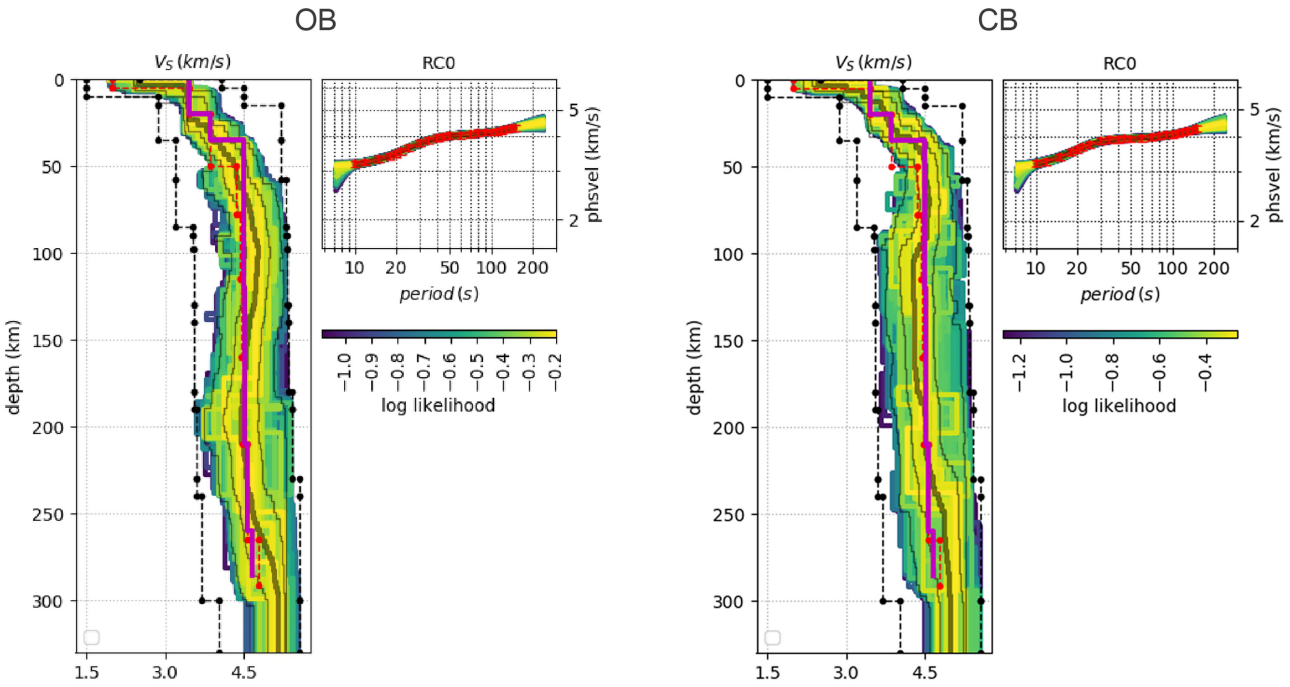

Figure 12. Results of the depth inversion under the OB (longitude 109°, latitude 38°) and under the Cathaysia Block (CB) (longitude 110°, latitude 25°). Dashed black models indicate the prior boundaries. Purple model denotes the ak135 continental model. Coloured models correspond to the 1000 best models with their corresponding dispersion curves. The colours correspond to log-likelihood values. Solid grey models indicate the median (thick line), 16 per cent and 84 per cent of the posterior distribution. The dispersion curves and error bars are displayed in red. RC0: phase velocity of the fundamental Rayleigh wave.

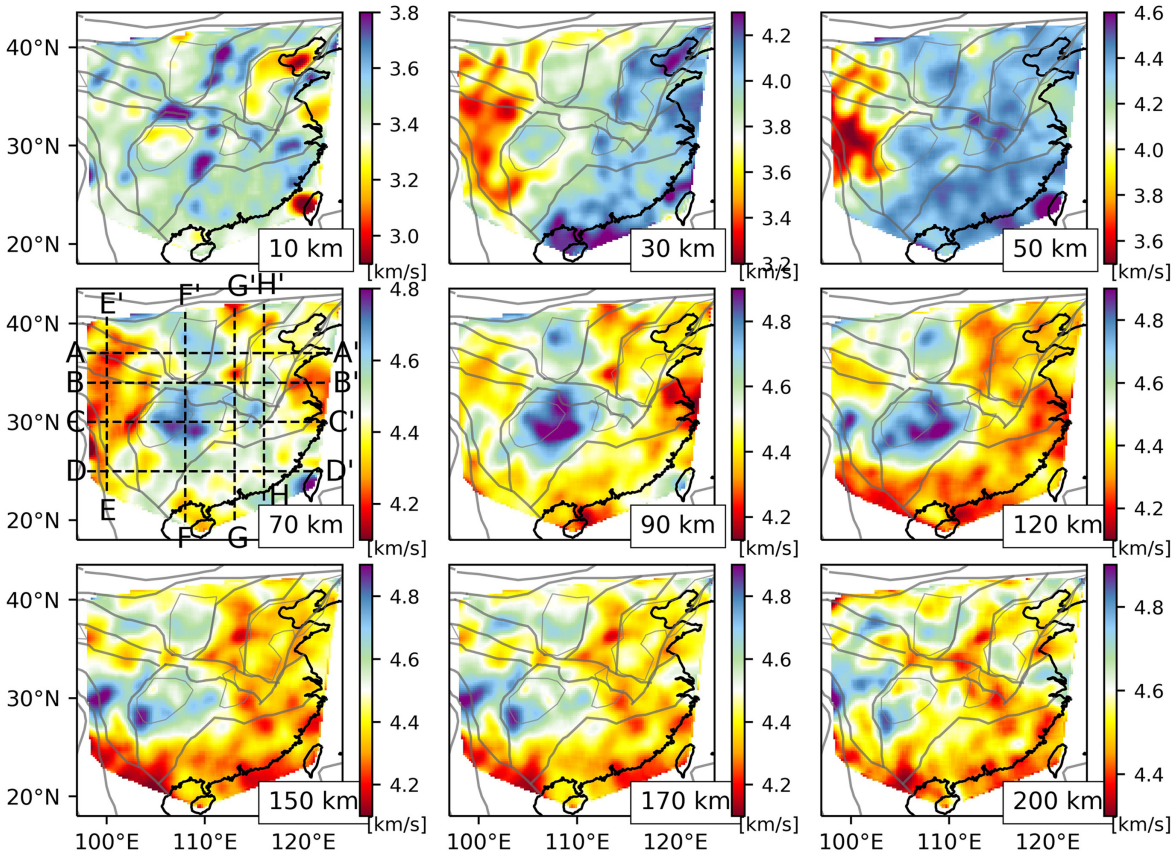

Figure 13. *S*-wave velocity anomaly maps at several depth from surface to 200 km. The contours of structural domains are the same as in Fig 1.

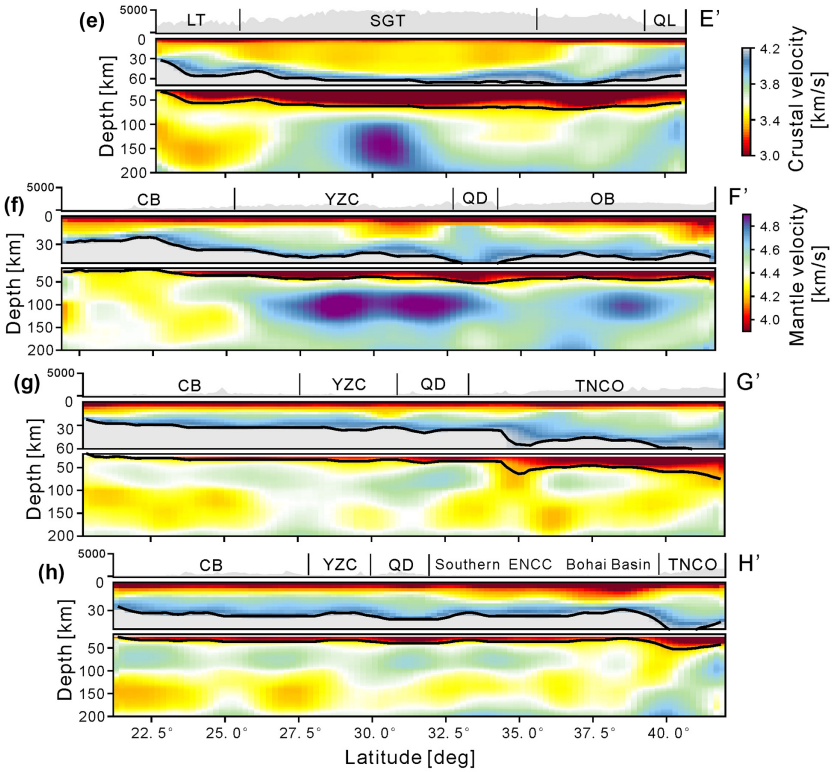

Figure 15. Vertical cross-sections of *S*-wave velocities along EE′ to HH′. Locations of these profiles are shown in Fig 13. Crustal thicknesses are denoted as black bold lines.

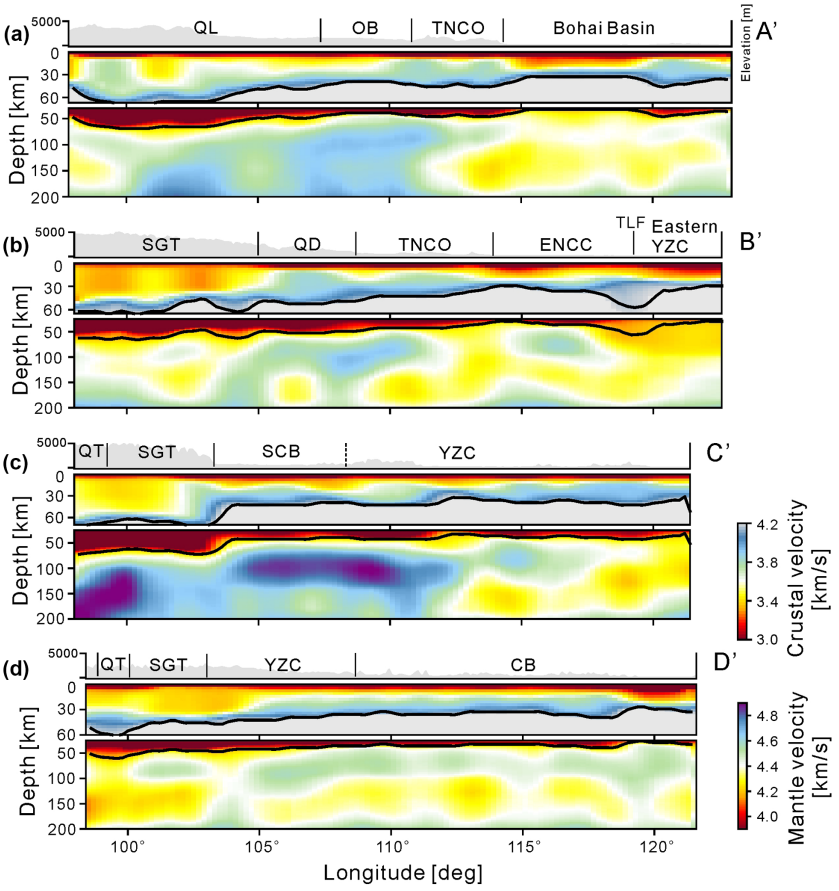

Figure 14. Vertical cross-sections of *S*-wave velocities along AA′ to DD′. Locations of these profiles are shown in Fig 13. Black bold lines denote the Moho.

are simply obtained by smoothing spline interpolation, avoiding solving a classical regularized inverse tomographic problem.

8.2 Destruction of the North China Craton

Cratons are continental regions where the Earth's lithosphere has remained largely stable since Archaean times. Cratons are characterized by thick depleted roots (usually > 200 km), fast seismic velocities, low heat flow and low density. Some cratons, such as the NCC and SCC have experienced lithosphere modification and destruction. Diamonds from Ordovician kimberlites in the ENCC provide evidence for the existence of a thick (∼ 200 km) and cold (∼ 40 mW m^{-2}) lithospheric mantle root. However, mantle xenoliths carried by Mesozoic–Cenozoic magmas in the ENCC indicate a thin, hot and fertile lithosphere (Menzies *et al.* 1993; Griffin *et al.* 1998).

Geological and geophysical investigations have revealed the widespread destruction of the ENCC lithosphere. The removal of ∼100 km of cratonic root, usually interpreted as triggered by the Mesozoic Pacific subduction (Niu 2005), has been confirmed by various local seismological studies (e.g. Chen *et al.* 2006, 2008; Huang *et al.* 2009; Bao *et al.* 2013). However, the extent and mechanism of the cratonic destruction is still controversial. Our phase-velocity maps suggest preserved cratonic keels under the NCC (HVA2) and SCC (HVA1). At longer periods (from 110 to 150 s), the HVAs HVA2 are clearly less pronounced than HVA1, which suggests a better preservation of the cratonic root in the YZC. The *S*-wave velocity model also shows a less pronounced cratonic root beneath the OB both in scale and amplitude (Figs 13–15). This could suggest a lithospheric destruction under the western NCC. Low velocities are broadly distributed in the eastern part of the TNCO, whereas the high velocities in the west suggest the effects of westwards subduction of the Palaeo-Pacific plate. Below the TNCO, LVAs underneath intermediate-velocity anomalies can be observed. This may imply the 'bottom-up' effects of lithospheric destruction by thermal/mechanical erosion. Our results agree with the recent mantle density study which concluded that most of the NCC lithosphere lost its cratonic signature (Xia *et al.* 2020). Overall, our model is consistent with a broadly distributed lithospheric root removal resulting from the Palaeo-Pacific subduction and roll-back, possibly reaching Mongolia and Russia, simultaneously as the NCC (Sheldrick *et al.* 2020).

8.3 The South China Craton

Although there is no direct geochemical evidence suggesting the destruction of the cratonic SCC lithosphere, xenoliths carried by the Mesozoic and Cenozoic basalts in the eastern and southern SCC indicate a thin and fertile lithospheric mantle (Huang & Xu 2010). Geophysical studies generally find a very similar lithospheric architecture for the eastern NCC and SCC, which would suggest that the eastern part of the SCC has undergone similar processes of lithospheric destruction (e.g. Li *et al.* 2018). As a consequence, one of the most salient features of the SCC is the intense Mesozoic igneous activity (Zhou & Li 2000). The spatial and temporal distribution of magmatism has been related to the flat subduction and roll back of the Palaeo-Pacific plate (Li & Li 2007).

In our phase-velocity maps and 3-D *S*-wave model, the SCC displays a relatively simple structure with a pronounced high-velocity core beneath the Sichuan basin and LVAs surrounding it (Figs 9 and 13–15). The thick cratonic roots beneath the Sichuan Basin have been evidenced from receiver functions (Hu *et al.* 2011; Zhang *et al.* 2018), surface wave tomography (Shen *et al.* 2016; Shan *et al.* 2017) and body wave tomography (Zhao *et al.* 2012), with proposed lithospheric thicknesses varying from 130 to > 300 km. If we consider an *S* wave of 4.5 km s^{-1} as the lower boundary of cratons (Zhou *et al.* 2012), the lithospheric thickness should be greater than 200 km (CC′ in Fig. 14 and FF′ in Fig. 5). Strong gradient at around 120–130 km beneath the Sichuan basin very likely reflects the internal layering of the cratonic core, as indicated by *S*-wave receiver functions (Zhang *et al.* 2018). The widespread LVAs in the CB and eastern YZC are also in good agreement with the relatively flat and thin lithosphere (60–100 km) imaged by receiver functions and surface wave tomography (Li *et al.* 2013a; Shan *et al.* 2017). The flat slab and roll back model is generally thought to be responsible for the broad LVAs in the SCC. Slab-triggered mantle upwelling may have erased the eastern and southern SCC lithosphere. The larger volume of the LVAs in the SCC compared to that in the NCC may be attributed to the different nature of the precambrian lithosphere (Zhao & Cawood 2012) and to the dehydration of the subducted plate (Xia *et al.* 2019).

9 CONCLUSION

The newly developed smoothing spline eikonal tomography approach was applied to the dense CEArray to obtain high-resolution Rayleigh-wave phase-velocity maps for central and eastern China for periods between 25 and 150 s. A 3-D shear wave model has been derived from these new phase-velocity maps. The phase-velocity maps and 3-D model are characterized by a fine spatial resolution with small-scale structures that can be correlated to known geological structures, such as narrow rift systems or preserved cratonic domains. Our model confirms the heterogeneous nature of the NCC and reveals with great detail the domains where the cratonic roots have been removed.

ACKNOWLEDGMENTS

We thank the editor Huajian Yao, reviewer Yonghua Li and Yong Zheng for their constructive and thoughtful comments that help to improve the manuscript. Seismic data used in this study come from the Data Management Centre of China National Seismic Network at Institute of Geophysics, China Earthquake Administration (doi:10.11998/SeisDmc/SN, http://www.seisdmc.ac.cn) and IRIS (https://www.iris.edu/hq/). This work is supported by the National Natural Science Foundation of China (42076071 and U1701641), the Key Special Project for Introduced Talents Team of the Southern Marine Science and Engineering Guangdong Laboratory (Guangzhou) (GML2019ZD0204), the China Scholarship Council (no. 201804910670), the Guangdong Research Foundation (2019BT02H594) and the Key Research and Development Plan of Hainan Province (ZDYF2020198).

DATA AVAILABILITY

The waveforms used to measure Rayleigh wave phase velocities are available at https://doi.org/10.5281/zenodo.5136336.

REFERENCES

Ai, S., Zheng, Y., He, L. & Song, M, 2019a. Joint inversion of ambient noise and earthquake data in the Trans-North China Orogen: on-going lithospheric modification and its impact on the Cenozoic continental rifting, *Tectonophysics,* **763,** 73–85.

Ai, S., Zheng, Y., Riaz, M. S., Song, M., Zeng, S. & Xie, Z, 2019b. Seismic evidence on different rifting mechanisms in southern and northern segments of the Fenhe-Weihe Rift zone, *J. geophys. Res.—Solid Earth,* **124**(1), 609–630.

Bao, X., Song, X. & Li, J, 2015. High-resolution lithospheric structure beneath Mainland China from ambient noise and earthquake surface-wave tomography, *Earth planet. Sci. Lett.,* **417,** 132–141.

Bao, X., Song, X., Xu, M., Wang, L., Sun, X., Mi, N. & Li, H. 2013. Crust and upper mantle structure of the North China Craton and the NE Tibetan Plateau and its tectonic implications,*Earth planet. Sci. Lett.,* **369,** 129–137.

Bensen, G. D., Ritzwoller, M. H., Barmin, M. P., Levshin, A. L., Lin, F., Moschetti, M. P. & Yang, Y, 2007. Processing seismic ambient noise data to obtain reliable broad-band surface wave dispersion measurements, *Geophys. J. Int.,* **169**(3), 1239–1260.

Cai, Y., Wu, J., Rietbrock, A., Wang, W., Fang, L., Yi, S. & Liu, J, 2021. S wave velocity structure of the crust and upper mantle beneath Shanxi Rift, Central North China Craton and its tectonic implications, *Tectonics,* **40**(4).

Chen, L., Tao, W., Zhao, L. & Zheng, T, 2008. Distinct lateral variation of lithospheric thickness in the Northeastern North China Craton, *Earth planet. Sci. Lett.,* **267**(1-2), 56–68.

Chen, L., Zheng, T. & Xu, W, 2006. A thinned lithospheric image of the Tanlu Fault Zone, eastern China: constructed from wave equation based receiver function migration, *J. geophys. Res.—Solid Earth,* **111**(B9).

Chevrot, S. & Lehujeur, M, 2022. Eikonal surface wave tomography with smoothing splines—application to Southern California, *Geophys. J. Int.,* **229**(3), 1927–1941.

Feng, L. & Ritzwoller, M. H, 2019. A 3-D shear velocity model of the crust and uppermost mantle beneath Alaska including apparent radial anisotropy, *J. geophys. Res.—Solid Earth,* **124**(10), 10468–10497.

Feng, M. & An, M, 2010. Lithospheric structure of the Chinese mainland determined from joint inversion of regional and teleseismic Rayleigh-wave group velocities, *J. geophys. Res.—Solid Earth,* **115**(B6).

Griffin, W. L., Andi, Z., O'reilly, S. Y. & Ryan, C. G, 1998. Phanerozoic evolution of the lithosphere beneath the Sino-Korean Craton, in *Mantle Dynamics and Plate Interactions in East Asia,* Vol. **27,** pp. 107–126.

Guo, Z., Gao, X., Li, T. & Wang, W, 2018. Crustal and uppermost mantle structures of the South China from joint analysis of receiver functions and Rayleigh wave dispersions, *Phys. Earth planet. Inter.,* **278,** 16–25.

Hao, S., Huang, Z., Han, C., Wang, L., Xu, M., Mi, N. & Yu, D, 2021. Layered crustal azimuthal anisotropy beneath the northeastern Tibetan Plateau revealed by Rayleigh-wave Eikonal tomography, *Earth planet. Sci. Lett.,* **563,** 116891.

Hariharan, A., Dalton, C. A., Babikoff, J. & Ekström, G, 2022. Controls on surface wave overtone interference, *Geophys. J. Int.,* **228**(3), 1665–1683.

Hariharan, A., Dalton, C. A., Ma, Z. & Ekström, G, 2020. Evidence of overtone interference in fundamental-mode Rayleigh wave phase and amplitude measurements, *J. geophys. Res.—Solid Earth,* **125**(1).

Herrmann, R.B. 2013. Computer programs in seismology: An evolving tool for instruction and research, *Seismological Research Letters,***84**(6),1081–1088..

Hu, J., Xu, X., Yang, H., Wen, L. & Li, G, 2011. S receiver function analysis of the crustal and lithospheric structures beneath eastern Tibet, *Earth planet. Sci. Lett.,* **306**(1-2), 77–85.

Huang, J. & Zhao, D, 2006. High-resolution mantle tomography of China and surrounding regions, *J. geophys. Res.—Solid Earth,* **111**(B9).

Huang, X. & Xu, Y, 2010. Thermal state and structure of the lithosphere beneath eastern China: a synthesis on basalt-borne xenoliths, *J. Earth Sci.,* **21**(5), 711–730.

Huang, Z., Li, H., Zheng, Y. & Peng, Y, 2009. The lithosphere of North China Craton from surface wave tomography, *Earth planet. Sci. Lett.,* **288**(1-2), 164–173.

Jiang, M., Ai, Y., Chen, L. & Yang, Y, 2013. Local modification of the lithosphere beneath the central and western North China Craton: 3-D constraints from Rayleigh wave tomography, *Gondwana Res.,* **24**(3-4), 849–864.

Kennett, B. L., Engdahl, E. R. & Buland, R, 1995. Constraints on seismic velocities in the Earth from traveltimes, *Geophys. J. Int.,* **122**(1), 108–124.

Lehujeur, M. & Chevrot, S, 2020a. Eikonal tomography using coherent surface waves extracted from ambient noise by iterative matched filtering—application to the large-N Maupasacq array, *J. geophys. Res.—Solid Earth,* **125**(6).

Lehujeur, M. & Chevrot, S, 2020b. On the validity of the eikonal equation for surface-wave phase-velocity tomography, *Geophys. J. Int.,* **223**(2), 908–914.

Lehujeur, M., Vergne, J., Schmittbuhl, J., Zigone, D., Le Chenadec, A. & Team, EstOF, 2018. Reservoir imaging using ambient noise correlation from a dense seismic network, *J. geophys. Res.—Solid Earth,* **123**(8), 6671–6686.

Li, H., Song, X., Lü, Q., Yang, X., Deng, Y., Ouyang, L. & Jiang, G, 2018. Seismic imaging of lithosphere structure and upper mantle deformation beneath east-central China and their tectonic implications, *J. geophys. Res.—Solid Earth,* **123**(4), 2856–2870.

Li, Q., Gao, R., Wu, F. T., Guan, Y., Ye, Z., Liu, Q. & Shen, X., 2013a. Seismic structure in the southeastern China using teleseismic receiver functions, *Tectonophysics,* **606,** 24–35.

Li, Y., Wu, Q., Pan, J., Zhang, F. & Yu, D., 2013b. An upper-mantle S-wave velocity model for East Asia from Rayleigh wave tomography, *Earth planet. Sci. Lett.,* **377,** 367–377.

Li, Z. X. & Li, X. H., 2007. Formation of the 1300-km-wide intracontinental orogen and postorogenic magmatic province in Mesozoic South China: a flat-slab subduction model, *Geology,* **35**(2), 179–182.

Liang, C., Song, X. & Huang, J., 2004. Tomographic inversion of Pn travel times in China, *J. geophys. Res. Solid Earth,* **109**(B11).

Lin, F. C. & Ritzwoller, M. H., 2011. Helmholtz surface wave tomography for isotropic and azimuthally anisotropic structure, *Geophys. J. Int.,* **186**(3), 1104–1120.

Lin, F. C., Ritzwoller, M. H. & Snieder, R., 2009. Eikonal tomography: surface wave tomography by phase front tracking across a regional broad-band seismic array, *Geophys. J. Int.,* **177**(3), 1091–1110.

Menzies, M. A., Fan, W. & Zhang, M., 1993. Palaeozoic and Cenozoic lithoprobes and the loss of>120 km of Archaean lithosphere, Sino-Korean craton, China, *Geol. Soc., London, Spec. Publ.,* **76**(1), 71–81.

Menzies, M. A. & Xu, Y., 1998. Geodynamics of the North China craton, in *Mantle Dynamics and Plate Interactions in East Asia,* Vol. **27,** pp. 155–165.

Montagner, J. P. & Kennett, B. L. N, 1996. How to reconcile body-wave and normal-mode reference Earth models, *Geophys. J. Int.,* **125**(1), 229–248.

Mosegaard, K. & Tarantola, A., 1995. Monte Carlo sampling of solutions to inverse problems, *J. geophys. Res.—Solid Earth,* **100**(B7), 12431–12447.

Niu, Y. L. 2005. Generation and evolution of basaltic magmas: some basic concepts and a new view on the origin of Mesozoic–Cenozoic basaltic volcanism in eastern China. *Geol. J. China Univ.,* **11**(1), 9–46.

Pandey, S., Yuan, X., Debayle, E., Priestley, K., Kind, R., Tilmann, F. & Li, X., 2014. A 3D shear-wave velocity model of the upper mantle beneath China and the surrounding areas, *Tectonophysics,* **633,** 193–210.

Shan, B., Xiong, X., Zhao, K. F., Xie, Z. J., Zheng, Y. & Zhou, L., 2017. Crustal and upper-mantle structure of South China from Rayleigh wave tomography, *Geophys. J. Int.,* **208**(3), 1643–1654.

Sheldrick, T. C., Barry, T. L., Dash, B., Gan, C., Millar, I. L., Barfod, D. N. & Halton, A. M., 2020. Simultaneous and extensive removal of the East Asian lithospheric root, *Sci. Rep.,* **10**(1), 1–6.

Shen, W., Ritzwoller, M. H., Kang, D., Kim, Y., Lin, F. C., Ning, J. & Zhou, L., 2016. A seismic reference model for the crust and uppermost mantle beneath China from surface wave dispersion, *Geophys. J. Int.,* **206**(2), 954–979.

Smith, W. H. F. & Wessel, P., 1990. Gridding with continuous curvature splines in tension, *Geophysics,* **55**(3), 293–305.

Tarantola, A. 2005. *Inverse Problem Theory and Methods for Model Parameter Estimation,* SIAM: Society for Industrial and Applied Mathematics, 978-0-89871-572-9.

Tromp, J. & Dahlen, F. A., 1992. Variational principles for surface wave propagation on a laterally heterogeneous Earth—I. Time-domain JWKB theory, *Geophys. J. Int.,* **109**(3), 581–598.

Wielandt, E. 1993. Propagation and structural interpretation of non-plane aves, *Geophys. J. Int.,* **113**(1), 45–53.

Wu, F. Y., Lin, J. Q., Wilde, S. A. & Yang, J. H., 2005. Nature and significance of the Early Cretaceous giant igneous event in eastern China, *Earth planet. Sci. Lett.,* **233**(1-2), 103–119.

Xia, B., Thybo, H. & Artemieva, I. M., 2020. Lithosphere mantle density of the North China Craton, *J. geophys. Res.—Solid Earth,* **125**(9).

Xia, Q. K., Liu, J., Kovács, I., Hao, Y. T., Li, P., Yang, X. Z. & Sheng, Y. M., 2019. Water in the upper mantle and deep crust of eastern China: concentration, distribution and implications, *Natl. Sci. Rev.,* **6**(1), 125–144.

Xu, J., Ben-Avraham, Z., Kelty, T. & Yu, H. S., 2014. Origin of marginal basins of the NW Pacific and their plate tectonic reconstructions, *Earth Sci. Rev.,* **130,** 154–196.

Xu, Z. J., Song, X. & Zhu, L., 2013. Crustal and uppermost mantle S velocity structure under Hi-CLIMB seismic array in central Tibetan Plateau from joint inversion of surface wave dispersion and receiver function data, *Tectonophysics,* **584,** 209–220.

Yin, A. 2006. Cenozoic tectonic evolution of the Himalayan orogen as constrained by along-strike variation of structural geometry, exhumation history, and foreland sedimentation, *Earth Sci. Rev.,* **76**(1-2), 1–131.

Yin, A. & Harrison, T. M., 2000. Geologic evolution of the Himalayan-Tibetan orogen, *Annu. Rev. Earth Planet. Sci.,* **28**(1), 211–280.

Zhang, A., Guo, Z., Afonso, J. C., Yang, Y., Yang, B. & Xu, Y., 2020. The deep thermochemical structure of the Dabie orogenic belt from multi-observable probabilistic inversion, *Tectonophysics,* **787,** 228478.

Zhang, Y. Y., Chen, L., Ai, Y. S., Jiang, M. M., Xu, W. W. & Shen, Z. Y., 2018. Lithospheric structure of the South China Block from S-receiver function, *Chin. J. Geophys.,* **61**(1), 138–149. (in Chinese). https://doi.org/10.6038/cjg2018L0226.

Zhao, G. & Cawood, P. A., 1999. Tectonothermal evolution of the Mayuan Assemblage in the Cathaysia Block; implications for Neoproterozoic collision-related assembly of the South China Craton, *Am. J. Sci.,* **299**(4), 309–339.

Zhao, G. & Cawood, P. A, 2012. Precambrian geology of China, *Precambrian Res.,* **222,** 13–54.

Zhao, G., Sun, M., Wilde, S. A. & Sanzhong, L., 2005. Late Archean to Paleoproterozoic evolution of the North China Craton: key issues revisited, *Precambrian Res.,* **136**(2), 177–202.

Zhao, L., Allen, R. M., Zheng, T. & Zhu, R., 2012. High-resolution body wave tomography models of the upper mantle beneath eastern China and the adjacent areas, *Geochem. Geophys. Geosyst.,* **13**(6).

Zheng, X. F., Yao, Z. X., Liang, J. H. & Zheng, J., 2010. The role played and opportunities provided by IGP DMC of China National Seismic Network in Wenchuan earthquake disaster relief and researches, *Bull. seism. Soc. Am.,* **100**(5B), 2866–2872.

Zheng, Y., Shen, W., Zhou, L., Yang, Y., Xie, Z. & Ritzwoller, M. H., 2011. Crust and uppermost mantle beneath the North China Craton, northeastern China, and the Sea of Japan from ambient noise tomography, *J. geophys. Res. Solid Earth,* **116**(B12).1–25.

Zhou, L., Xie, J., Shen, W., Zheng, Y., Yang, Y., Shi, H. & Ritzwoller, M. H., 2012. The structure of the crust and uppermost mantle beneath South China from ambient noise and earthquake tomography, *Geophys. J. Int.,* **189**(3), 1565–1583.

Zhou, X. M. & Li, W. X., 2000. Origin of Late Mesozoic igneous rocks in Southeastern China: implications for lithosphere subduction and underplating of mafic magmas, *Tectonophysics,* **326**(3-4), 269–287.

Zhu, R., Xu, Y., Zhu, G., Zhang, H., Xia, Q. & Zheng, T., 2012. Destruction of the North China craton, *Sci. China Earth Sci.,* **55**(10), 1565–1587.